Jiao et al. *Microsystems & Nanoengineering* (2026)12:88
https://doi.org/10.1038/s41378-026-01202-7

Microsystems & Nanoengineering
www.nature.com/micronano

ARTICLE Open Access

A laminated magnetic flux concentrator with low coercivity and high relative permeability for efficient flux modulation in MEMS magnetoresistive sensors

Qifeng Jiao[1,2], Guoshuo Peng[1,2], Zhenhu Jin[1,2]✉, Chenglong Zhang[1] and Jiamin Chen[1,2,3]✉

Abstract

The detectivity of magnetic tunnel junction (MTJ) sensors cannot be improved further because of the existence of 1/*f* noise. Micro - electromechanical systems (MEMS) integrated with magnetic flux concentrators (MFCs) can be an effective approach to suppressing 1/*f* noise for modulating low-frequency magnetic fields. The challenge in fabricating small-sized and low-noise MTJ-MEMS hybrid magnetic sensors is associated with the production of high-performance MFCs. For the preparation of MFCs applicable to MTJ-MEMS hybrid magnetic sensors, in this research, a novel Ta/$Ni_{77}Fe_{14}Cu_5Mo_4$ laminated structure was adopted to decrease the coercivity of the magnetic film dozens of times. Also, through optimizing the sputtering power, a relative permeability of 3246 was attained. The simulation outcomes demonstrated that the MTJ-MEMS hybrid magnetic sensor which utilized this magnetic film had a modulation efficiency of 65.4%, and it retained a competitive edge among similar magnetic sensors. A sensor prototype was successfully developed with 400-nm- thick MFCs by optimizing the fabrication process, and the MTJ's sensitivity was increased by 2.2 times. In comparison to low-frequency noise, the high-frequency noise of the MTJ showed a reduction in noise power spectral density by a factor of 686. MTJ sensors will be highly competitive candidates in the field of ultra-weak magnetic field detection because of these results.

Introduction

Magnetic sensors have been widely used in a variety of fields like defense[1,2], transportation[3–5], and biomedical engineering[6–8]. In recent decades, a great many kinds of magnetic sensors have been created, for instance, induction coils[9,10], optically pumped magnetometers[11], superconducting quantum interference devices (SQUIDs)[12], fluxgate sensors[13], Hall sensors[14], anisotropic magnetoresistance (AMR) sensors[15], giant magnetoresistance (GMR) sensors[16], and magnetic tunnel junctions (MTJs)[17]. Among these, MTJs stand out in the detection of weak magnetic fields because of their small size, low power consumption, and high sensitivity. Nevertheless, 1/*f* noise has a severe impact on MTJs, leading to low detectivity at low frequencies. Several methods have been investigated to lessen the impact of 1/*f* noise, such as chopper modulation[18–20], AC polarity reversal modulation[21,22], integrated superconducting loops[23,24], integrated magnetic flux concentrators (MFCs)[25,26], and integrated MEMS-based flux concentrators[27–29]. The utilization of chopper modulation demands the employment of large magnetic shielding tubes for periodically shielding external magnetic fields, which may lead to the deterioration of the sensor's spatial resolution. The AC polarity reversal modulation functions by imposing an AC magnetic field that is orthogonal to the sensitive axis of the magnetoresistive element, thus shifting the power spectral density

Correspondence: Zhenhu Jin (jinzhenhu@aircas.ac.cn) or Jiamin Chen (chenjm@aircas.ac.cn)
[1]State Key Laboratory of Transducer Technology, Aerospace Information Research Institute, Chinese Academy of Sciences, Beijing 100190, China
[2]School of Electronic, Electrical and Communication Engineering, University of Chinese Academy of Sciences, Beijing 100049, China
Full list of author information is available at the end of the article

of the target magnetic field towards higher frequencies. Nevertheless, to generate the AC magnetic field, this approach demands the application of an AC current to copper wires, and this may bring in extra magnetic noise. According to the Meissner effect, superconducting loops can amplify local magnetic flux density around magnetoresistive components by hundreds of times, significantly improving the sensitivity of magnetoresistive devices. Nevertheless, superconducting loops need to work in extremely low—temperature conditions, which enlarges the size of the system and boosts its power consumption.

In recent years, researchers have paid great attention to MFCs which are able to work at room temperature. The MFC, fabricated from soft magnetic materials with high permeability, is able to magnify the magnetic flux close to the magnetoresistive sensor, thus increasing its sensitivity. Aiming at achieving small sensor sizes, numerous magnetoresistive sensors with integrated MFCs have been developed, resulting in several-fold improvements in sensitivity[30,31]. Considering that the magnetic field gain of current micron-scale flux concentrators has reached a bottleneck, researchers have proposed integrating MEMS with the flux concentrators, which could reduce the noise of magnetoresistive sensors by several hundred times[32,33], thereby suppressing the noise level of the magnetoresistive sensors to the pT level. Unfortunately, most of the reported MEMS-based flux concentrators have relatively low modulation efficiency[34–36]. In the past two years, the IEEC laboratory in Spain has developed an MTJ-MEMS hybrid sensor suitable for detecting space magnetic fields using a vertical motion modulation scheme. The modulation efficiency of the sensor is approximately 36%[37], and there is still considerable room for improvement. This is because the flux concentrator, which is part of the modulation structure, is located at a short distance from the magnetoresistive sensor, limiting the amplitude of the MEMS. Nevertheless, when the distance between the flux concentrator and the sensor is too large, the magnetic field gain will be decreased. Consequently, in practical design work, it is crucial to keep a proper distance between the flux concentrator and the sensor so as to attain high modulation efficiency while also retaining an adequate magnetic field gain.

Previously, in order to enhance the low-frequency magnetic field detectivity of MTJs, the author proposed a two-dimensional synchronous motion modulation (TDSMM) scheme based on a comb-driven resonator[38]. This scheme decreased the fabrication complexity of the composite magnetoresistive sensor while attaining high modulation efficiency. Nevertheless, because of manufacturing restrictions, the device failed to be successfully fabricated. The primary factor was the rather low permeability of the soft magnetic material for the flux concentrator fabrication, which impeded the efficient enhancement of the magnetoresistive element's sensitivity. Based on this, the current study explores the combination of a flux concentrator and an MTJ for magnetic flux adjustment. The $Ni_{77}Fe_{14}Cu_5Mo_4$ is used to make the flux concentrator so as to improve the MTJ's sensitivity. The soft magnetic film's coercivity is decreased by using a lamination structure. The effect of sputtering power on the hysteresis loop of the soft magnetic film is investigated to find the best sputtering conditions. The fabrication process of MFCs is optimized, and the MTJ is successfully integrated with MFCs. It has been demonstrated by experimental findings that MFCs with a thickness of 400 nm can achieve a magnetic field gain of 2.2 times. Moreover, finite-element simulations of the relevant scheme with this thickness indicate a modulation efficiency of 65.4%, which is still competitive in comparison with similar devices. The MTJ based on the integrated flux concentrator presented in this research is likely to enable the successful implementation of the TDSMM scheme. It is anticipated that the future integration of these devices with MEMS structures will improve the low-frequency field detection capabilities.

Design and simulation

Figure 1 shows the sensor model. There are two MFCs in the model, whose short side measures 30 μm and long side is 492 μm. There is an MTJ which lies in the space between the two MFCs, and the MTJ is 12 μm away from the MFCs. The MTJ along the x-axis and the MFCs in the y-axis direction, respectively, perform oscillations and periodic motion for the TDSMM. The modulation shifts the target DC or low-frequency magnetic signal to the high-frequency band.

The noise of the MTJ is given by Eq. (1)[39]:

$$S_B{}^{MTJ}(\mathrm{T}/\sqrt{\mathrm{Hz}}) = \frac{1}{IS_0}\sqrt{2qIR^2\ \coth\left(\frac{qV}{2k_BT}\right) + \frac{\alpha I^2R^2}{Af^\gamma}} \tag{1}$$

where $S_B{}^{MTJ}$ denotes the power spectral density of the noise in the MTJ, and I stands for the bias current. The sensitivity of the MTJ is indicated by S_0, which has units of Ω/T. The bias voltage is V, the Boltzmann constant is k_B, and the temperature is T. The Hooge-like parameter is α, the sensing area of the MTJ is represented by A, the frequency is f, and γ is the $1/f$ fitting parameter. It can be seen from Eq. (1) that enhancing the MTJ's sensitivity and adjusting the external magnetic field to higher frequencies are beneficial for suppressing the MTJ's $1/f$ noise.

Given that the amplification of the magnetic flux density by MFCs is associated with their dimensions and relative permeability, this paper initially examines how size and relative permeability influence the magnetic field gain of

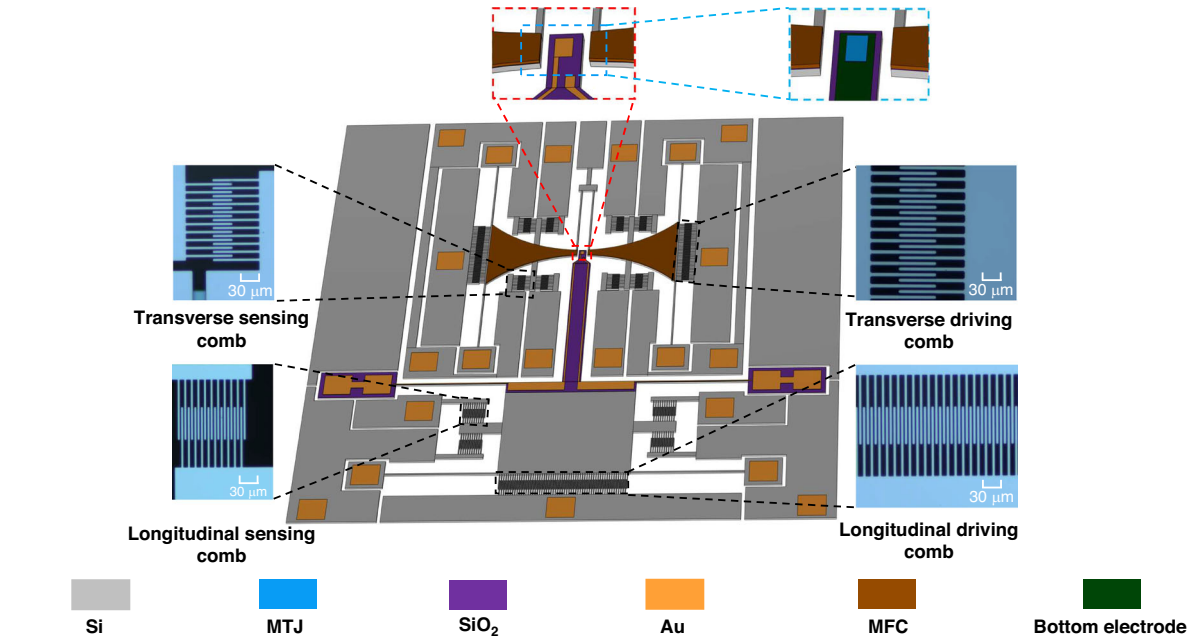

Fig. 1 Schematic diagram of a hybrid device. Conceptual illustration of the integrated MTJ-MEMS sensing device

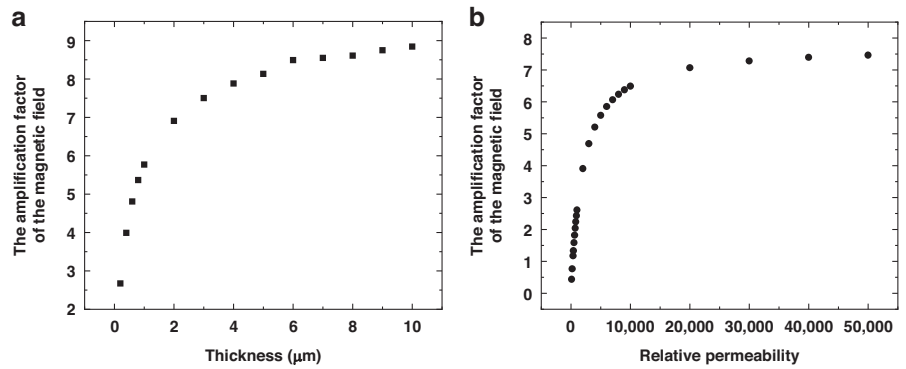

Fig. 2 The amplification factor of the magnetic field within the gap for MFCs. Magnification of magnetic field in the gap of MFCs (**a**) at different thicknesses; (**b**) under different relative permeabilities

MFCs. In Fig. 2a, the variation curve of the magnetic field amplification factor within the gap in relation to the thickness of MFCs is presented. It can be seen from the results that the magnetic field amplification is related to the thickness of MFCs in a certain proportion. As the thickness of MFCs grows to 4 μm, the growth rate of the magnetic field gain slows down and shows a tendency to reach saturation. Moreover, an excessive thickness can lead to a rise in the device-making complexity. Consequently, during the actual manufacturing process, the thickness of MFCs is defined as 400 nm. As shown in Fig. 2b, when the MFCs have a thickness of 400 nm, one can observe the variation curve of the magnetic field gain in the gap in relation to the relative permeability. If the relative permeability is lower than 600, the magnetic field in the gap fails to be effectively amplified. It shows that in order to get MFCs which are suitable for the TDSMM plan, the relative permeability of the made magnetic film should be more than 600. This guarantees a distinct gradient of the magnetic field amplification factor along the MTJ's sensitive axis, which enables the vibrating MFCs to produce a greater modulated magnetic field amplitude, thus enhancing the modulation efficiency of the TDSMM.

Moreover, the finite element method was utilized to simulate the modulation efficiency of the TDSMM scheme. In this case, the thickness of the MFC is 400 nm and its relative permeability is 3246. The distance between

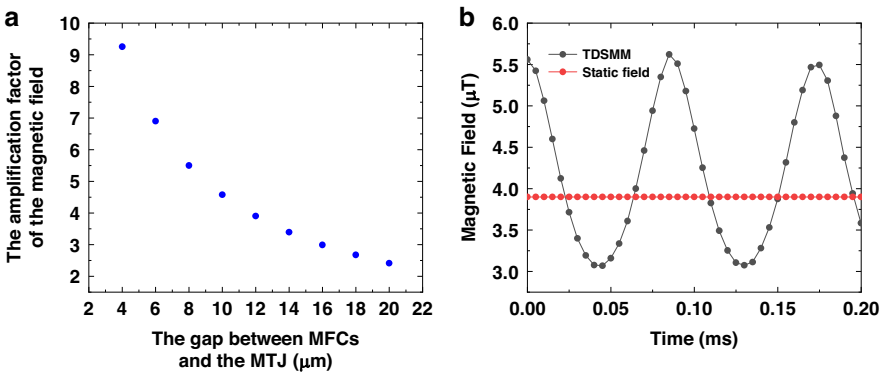

Fig. 3 Finite element simulation of the modulated magnetic field. a The relationship between magnetic field gain and the distance between MFCs and the MTJ. **b** Modulation magnetic fields of TDSMM

Table 1 Comparison of modulation efficiency of different types of magnetoresistive-MEMS hybrid magnetic sensors

Modulation Schemes	Magnetioresistive Elements	Modulation Efficiency (%)
Micro-cantilever[34]	GMR	0.11
Micro-torsionator[39]	MTJ	11
Piezoelectric resonator[49]	GMR	13
VMFM[37]	MTJ	36
MTJ motion modulation[36]	MTJ	8.69
TDSMM (this work)	MTJ	65.4

MFCs and the MTJ is set to 12 μm. When the distance between MFCs and the MTJ changes, the variation of the magnetic field gain is shown in Fig. 3a. As can be seen from Fig. 3a, the magnetic field gain exhibits a sharp upward trend with decreasing spacing; however, a smaller spacing imposes inherent constraints on the resonator's oscillation amplitude, which in turn reduces the magnitude of the modulated magnetic field and compromises modulation efficiency. Conversely, an excessively large spacing not only diminishes the static magnetic field gain but also weakens the coupling effect of the connecting beams—the component specifically designed to synchronize the motion of the two transverse masses. This weakened coupling leads to asynchronous motion between the transverse masses, resulting in distortion of the modulated magnetic field waveform. Therefore, the selection of 12 μm as the optimal spacing represents a comprehensive trade-off among three critical performance metrics: resonator oscillation amplitude, magnetic field gain, and the waveform integrity of the modulated magnetic field.

The vibration frequencies of MFCs and the MTJ are consistent with those of the transverse ($f_1 = 11570$ Hz) and longitudinal resonators ($f_2 = 5785$ Hz), respectively. Figure 3b presents the simulation results of the modulated magnetic field. MFCs can produce an amplified static field of 3.9 μT when they are exposed to a 1 μT external field. The MTJ and MFCs, through their coordinated movement, can upconvert the magnetic field into a high-frequency alternating signal which is close to the ideal sinusoidal form. The magnitude of the alternating magnetic field reaches 2.55 μT. The modulation efficiency of the MFCs (designed in this paper for the TDSMM scheme) is around 65.4% according to these results. Among hybrid magnetoresistive sensors of similar types, this figure is still highly competitive. Table 1 compares the modulation efficiency of various magnetoresistive-MEMS sensors. By proportionally increasing the size of MFCs, the peak-to-peak value of the modulated magnetic field can be increased, thereby enhancing the modulation efficiency. It should be noted that an increase in the size of MFCs will lead to an increase in the size of the resonator. At this point, to ensure that the resonator has a sufficiently large displacement, the amplitude of the resonator excitation voltage needs to be increased.

Experimental process

Considering that the TDSMM structure contains two sets of resonators, it is necessary to isolate them. Therefore, this article selects silicon-on-insulator (SOI) wafers as the substrate for MTJ multilayer films. The MTJ stack structure employed in this work consists of the following layers, from bottom to top: Ta/Ru/Ta/Ru/Ta/Ru/IrMn/CoFe/Ru/CoFeB/MgO/CoFeB/Ru/NiFe/Ta/Ru.

The CoFe/Ru/CoFeB layers serve as the artificial antiferromagnetic (AFM) layer, with IrMn inducing antiparallel alignment of magnetic moments. The CoFeB/Ru/NiFe (free layer) exhibits field-dependent magnetization rotation. The reference and pinned layers in the AFM

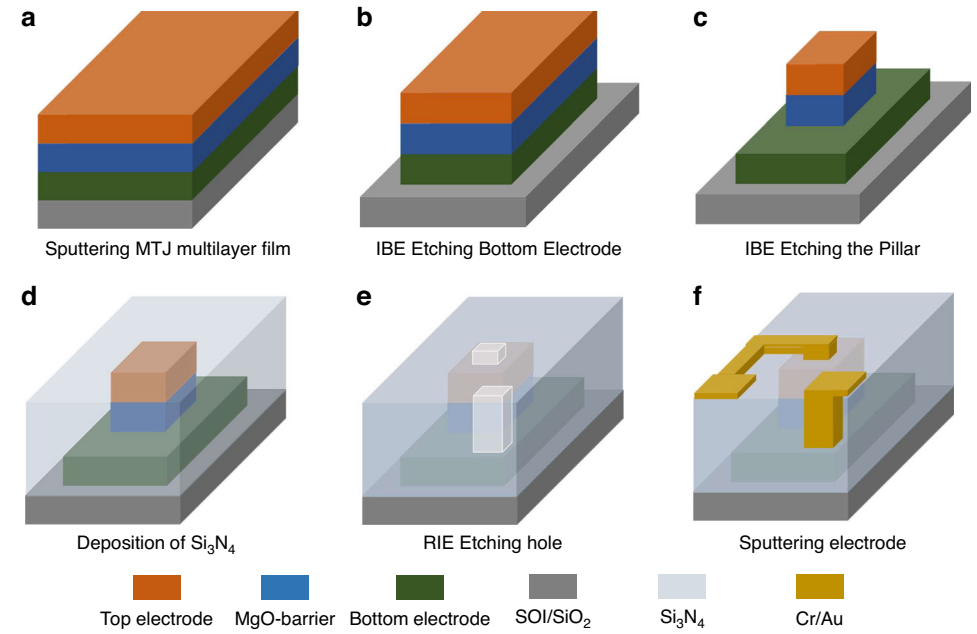

Fig. 4 The processing procedure of the MTJ sensor. Schematic diagram of the MTJ fabrication process: **a** Deposition of MTJ multilayer film; **b** Define the bottom electrode using ion beam etching; **c** Pillar etching using ion beam etching; **d** Deposition of Si_3N_4; **e** Opening of connections using reactive ion etching; **f** Sedimentation of Cr (30 nm)/Au (300 nm)

structure correspond to CoFeB and CoFe, respectively. Orthogonal magnetization configuration between fixed and free layers, realized via sequential annealing, enables broader linear response in the sensor[40]. The coercivity suppression in the free layer results from NiFe integration within the CoFeB/Ru/NiFe AFM multilayer[41], effectively addressing hysteresis concerns. The CoFeB/MgO interface enables coherent electron tunneling, yielding a high magnetoresistive ratio in the MTJ device[42].

The MTJ operates on the principle of electron tunneling across the insulating barrier, establishing a current flow in the perpendicular-to-plane direction. Fabrication requires four photolithographic stages: initial patterning of the bottom electrode via ion beam etching, followed by pillar structure definition. Following the initial two photolithography processes, a 300 nm-thick Si_3N_4 is deposited using inductively coupled plasma chemical vapor deposition (ICP-CVD) to protect the the MTJ. Next, a reactive ion etching (RIE) process is employed to open connections to the bottom and top electrodes of the MTJ. Finally, Cr (30 nm)/Au (300 nm) is sputtered as the electrodes. The complete process steps are shown in Fig. 4.

$Ni_{77}Fe_{14}Cu_5Mo_4$, a soft magnetic alloy with high magnetic permeability, is the material for MFCs. The soft magnetic film was deposited via direct current magnetron sputtering, with the sputtering power adjusted to 100 W and the sputtering pressure being 0.73 Pa. During the film-forming process, a 120 Oe magnetic alignment field was applied to MFCs so as to endow them with uniaxial anisotropy. Moreover, in order to decrease the coercivity of MFCs, a 5 nm-thick Ta was laminated together with a 50 nm-thick $Ni_{77}Fe_{14}Cu_5Mo_4$. To confirm the formation of a laminated structure between Ta and $Ni_{77}Fe_{14}Cu_5Mo_4$, transmission electron microscopy (TEM) was employed to characterize the 6-layer structure, with the results presented in Fig. 5. As observed from the TEM images, Ta and $Ni_{77}Fe_{14}Cu_5Mo_4$ layers are alternately stacked, with individual thicknesses of approximately 5 nm and 50 nm, respectively.

Results and discussion

The influence of the Ta (5 nm)/$Ni_{77}Fe_{14}Cu_5Mo_4$ (50 nm) laminated structure on the hysteresis loop (shown in Fig. 6a, b) was initially explored. The hysteresis loop of the laminated structure is obtained through the vibrating sample magnetometer (VSM). The electromagnet in the VSM generates a uniform magnetic field to magnetize the laminated structure. The vibrating head causes the laminated structure to undergo periodic motion, resulting in a change in the magnetic flux in the pickup coil and generating a weak induced signal. These signals are processed by the phase-locked amplifier, and the hysteresis loop is derived by analyzing the signal parameters under the known magnetic field strength and vibration parameters[43]. It has been found that as the quantity of Ta (5 nm)/$Ni_{77}Fe_{14}Cu_5Mo_4$ (50 nm) stack

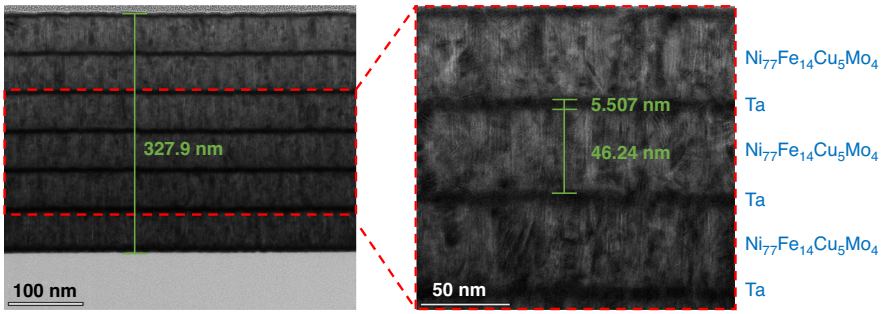

Fig. 5 TEM image of the laminated film. The TEM image of Ta/$Ni_{77}Fe_{14}Cu_5Mo_4$ six-layer structure

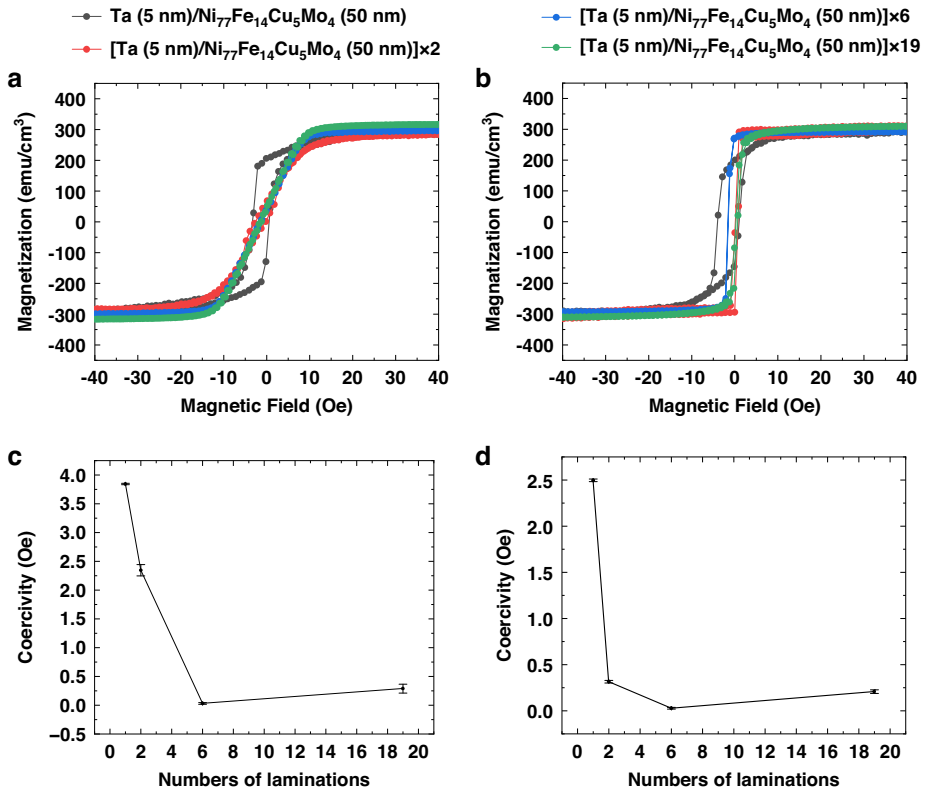

Fig. 6 The influence of the number of laminations on the hysteresis loop. Hysteresis loops of soft magnetic thin films with different numbers of laminations: **a** in the hard axis; **b** in the easy axis. The relationship between the coercivity of the magnetic film and the number of laminations: **c** in the hard axis; **d** in the easy axis

layers rises from one layer to multiple layers, the coercivity of the films drops considerably. Particularly, in the hard-axis direction (illustrated in Fig. 6c), the coercivity of a single-layer Ta (5 nm)/$Ni_{77}Fe_{14}Cu_5Mo_4$ (50 nm) film is 3.85 Oe; for a two-layer stack, [Ta (5 nm)/$Ni_{77}Fe_{14}Cu_5Mo_4$ (50 nm)] × 2, the coercivity reduces to 2.3 Oe. When the number of layers goes up to six, the coercivity of [Ta (5 nm)/$Ni_{77}Fe_{14}Cu_5Mo_4$ (50 nm)] × 6 experiences a sharp drop to 0.03 Oe. Nevertheless, once the stack reaches 19 layers, namely [Ta (5 nm)/$Ni_{77}Fe_{14}Cu_5Mo_4$ (50 nm)]×19, the coercivity ascends once more to 0.28 Oe. The behavior of the hysteresis loop in the easy-axis direction is similar to that in the hard-axis direction (illustrated Fig. 6d). In the case of a single-layer Ta/$Ni_{77}Fe_{14}Cu_5Mo_4$ film, the coercivity has a value of 2.496 Oe. In the [Ta (5 nm)/$Ni_{77}Fe_{14}Cu_5Mo_4$ (50 nm)]×2 stack, the coercivity goes down to 0.315 Oe. When the number of layers rises to six, in the [Ta (5 nm)/$Ni_{77}Fe_{14}Cu_5Mo_4$ (50 nm)]×6 stack, there is a remarkable decrease in coercivity to 0.027 Oe. When it comes to

[Ta (5 nm)/$Ni_{77}Fe_{14}Cu_5Mo_4$ (50 nm)]×19, the coercivity rises back to 0.219 Oe. The magnetic properties of the film may be affected by the slight internal tearing inside the film when the number of stack layers rises. This could be the reason for the observed behavior.

The magnetic hysteresis loop experiences complex changes as the number of Ta/$Ni_{77}Fe_{14}Cu_5Mo_4$ layers rises, and the coercivity has a particularly sharp decrease when there are six layers, which shows this trend. The possible cause of this situation might be associated with the vanishing of stripe-like magnetic domains. In a single-layer magnetic film, the magnetic domains' magnetization diverges from the substrate, showing a certain vertical component[44,45]. Upon the application of an external magnetic field, the magnetization behavior of these domains becomes inconsistent, resulting in higher coercivity. With an increase in the number of Ta/$Ni_{77}Fe_{14}Cu_5Mo_4$ layers, the antiferromagnetic coupling between adjacent magnetic layers is significantly enhanced, as the Ta spacer layers facilitate the transmission of exchange coupling interactions to promote the alignment of magnetization vectors in adjacent $Ni_{77}Fe_{14}Cu_5Mo_4$ layers, which effectively suppresses the formation of stripe domains by minimizing the magnetic energy associated with out-of-plane magnetization components and leads to a more uniform in-plane magnetic domain structure, thereby making the magnetization reversal process more coherent, reducing the energy barrier for domain wall motion, and resulting in a substantial decrease in coercivity[31,44]. When the number of layers exceeds six, the coercivity begins to rise slightly, dominated by the accumulation of structural stress in the laminated films: during the deposition process, each Ta/$Ni_{77}Fe_{14}Cu_5Mo_4$ bilayer introduces intrinsic residual stress due to lattice mismatch between the Ta spacer and $Ni_{77}Fe_{14}Cu_5Mo_4$ magnetic layer, as well as thermal stress induced by differences in thermal expansion coefficients; with the increase in layer count (especially when reaching 19 layers), the cumulative stress exceeds the yield strength of the film, leading to the formation of microcracks and slight internal delamination at the interface between layers, which reduce the overall compactness of the laminated structure and introduce additional pinning sites for domain walls (e.g., crack edges, interface gaps); during magnetization reversal, domain walls are trapped by these defects, requiring higher external magnetic fields to overcome the pinning effect, ultimately resulting in a slight increase in coercivity for the 19-layer sample.

The stripe domains' formation has a connection with the magnetic film's thickness[46]:

$$t_c = 2\pi\sqrt{\frac{A_{ex}}{K_\perp}} \tag{2}$$

The critical thickness is represented by t_c in Eq. (2). The exchange constant is denoted by A_{ex}, while the perpendicular anisotropy constant is represented by $K_\perp$. When the thickness of the magnetic film is greater than the critical thickness, stripe domain formation takes place. Consequently, in the laminated construction, it is essential to make sure that the thickness of a single magnetic layer is smaller than the critical thickness. The hysteresis loops of laminated films with single-layer $Ni_{77}Fe_{14}Cu_5Mo_4$ films having thicknesses of 150 nm and 50 nm are compared in Fig. 7. In Fig. 7, one can observe that in the laminated film where the single-layer $Ni_{77}Fe_{14}Cu_5Mo_4$ has a thickness of 150 nm, the saturation field is around 395 Oe and the coercivity is ~38 Oe. It shows that the laminated film in Fig. 7a still has a large number of stripe domains. As can be seen in Fig. 7b, when the thickness of the single-layer $Ni_{77}Fe_{14}Cu_5Mo_4$ is decreased to 50 nm, both the saturation field and coercivity of the laminated film are reduced markedly. The saturation field of the easy axis is around 2 Oe, and the coercivity is about 0.027 Oe. This implies that merely depending on the antiferromagnetic coupling between magnetic layers is not

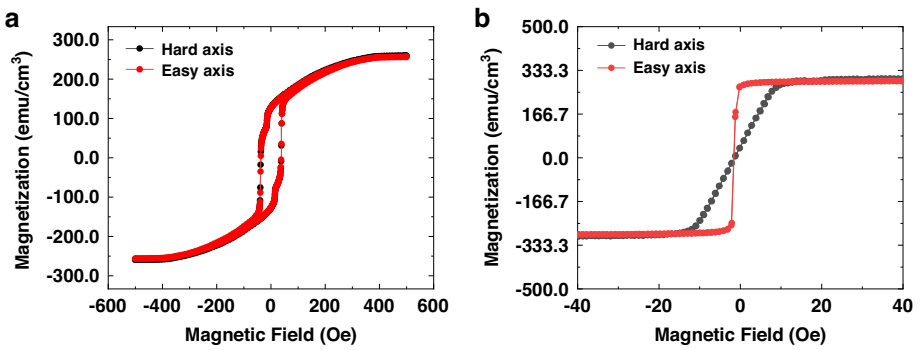

Fig. 7 The influence of laminate film thickness on the hysteresis loop. Hysteresis loops of different laminated magnetic films: **a** the laminated structure is [Ta (10 nm)/$Ni_{77}Fe_{14}Cu_5Mo_4$ (150 nm)]×3/Ta(10 nm); **b** the laminated structure is [Ta (5 nm)/$Ni_{77}Fe_{14}Cu_5Mo_4$ (50 nm)] × 6/Ta (5 nm)

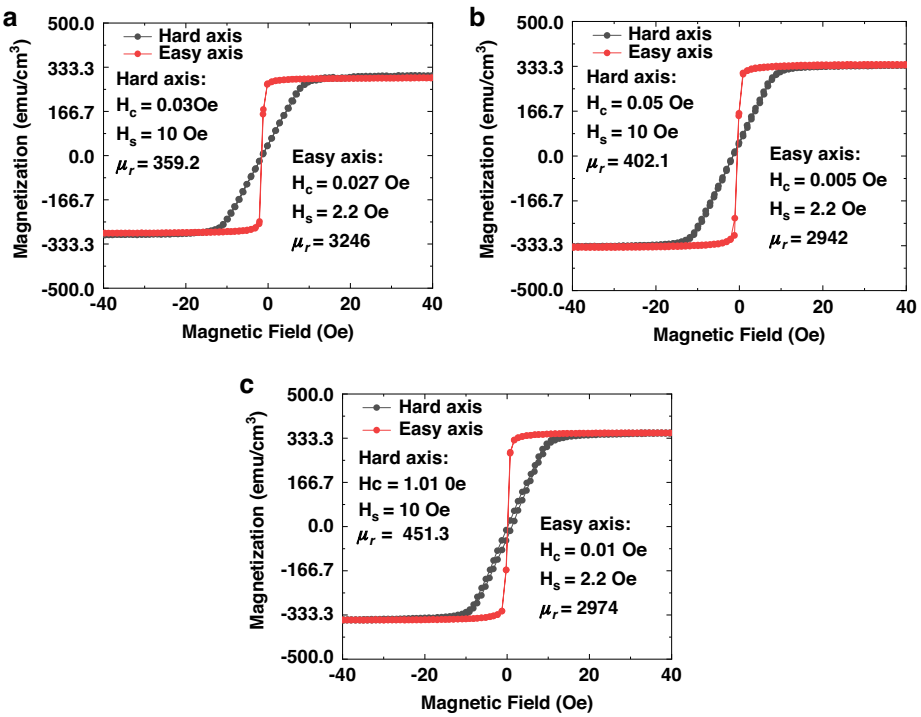

Fig. 8 The influence of power on the hysteresis loop. Hysteresis loops of soft magnetic thin films at different sputtering powers: **a** 100 W; **b** 130 W; **c** 160 W. The number of laminations for all magnetic films is 6

enough to cut down the stripe domains within the magnetic film; the thickness of the single magnetic layer has to be smaller than the critical thickness as well. Typically, a substantial reduction in stripe domains can be achieved by decreasing the thickness of the single-layer magnetic film. Meanwhile, the addition of the laminated structure gives rise to interlayer antiferromagnetic coupling among adjacent ferromagnetic layers[47,48], which has an effective suppression on the formation of stripe domains. Consequently, the saturation field and coercivity of the soft magnetic film are decreased to a large extent.

The magnetic properties of magnetic films are greatly affected by power. Therefore, during the sputtering process of $Ni_{77}Fe_{14}Cu_5Mo_4$ alloy, the influence of power on the hysteresis loops of magnetic films was further explored. Hysteresis loops were plotted in Fig. 8 for samples sputtered under various power conditions (all samples had 6 laminated layers). In Fig. 8, it can be seen that under all the three power conditions, the relative permeability in the direction of the easy axis is far larger than that in the direction of the hard axis. According to the results of the simulation in Section 2, for the magnetic field in the gap of MFCs to be effectively enhanced, the relative permeability of MFCs should be more than 600. For this study, the easy axis was chosen for the amplification of the magnetic field.

At a sputtering power of 100 W, the coercivity of the easy axis of the sample was 0.027 Oe; when the power increased to 130 W, the coercivity of the easy axis rose to 0.005 Oe; and at 160 W, the coercivity of the easy axis further increased to 0.01 Oe. It can be observed that under all three sputtering powers, the easy axis of the magnetic films exhibited very low coercivity (0.005 ~ 0.027 Oe). However, with the increase in sputtering power, the relative permeability of the films slightly decreased, which may be attributed to the higher energy carried by the atoms at higher powers, leading to the accumulation of larger internal stresses within the film. This could cause slight internal cracking or tearing of the film. The surface roughness of the [Ta (5 nm)/$Ni_{77}Fe_{14}Cu_5Mo_4$ (50 nm)]×6/Ta (5 nm) laminated structure under different sputtering powers was characterized using an atomic force microscope (AFM). The results are shown in Fig. 9. As the sputtering power increased, the surface roughness of the laminated structure gradually increased, indicating that the compactness of the film gradually deteriorated, which led to a slight decrease in the relative permeability of the film. To achieve the maximum relative permeability of MFCs, a sputtering power of 100 W will be employed for the integration of MFCs adjacent to the MTJ device in subsequent fabrication processes.

Table 2 summarizes key magnetic parameters of MFCs in different magnetoresistive-MEMS composite magnetic

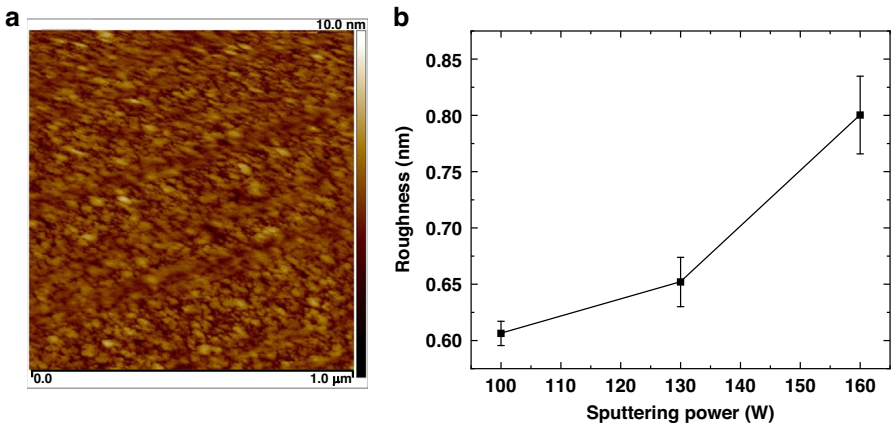

Fig. 9 The surface roughness of the laminated film. a 2D AFM image of [Ta (5 nm)/$Ni_{77}Fe_{14}Cu_5Mo_4$ (50 nm)] × 6/Ta (5 nm) at a sputtering power of 100 W. **b** The relationship between the surface roughness of [Ta (5 nm)/$Ni_{77}Fe_{14}Cu_5Mo_4$ (50 nm)] × 6/Ta (5 nm) and the sputtering power

Table 2 Performance comparison of different MFCs in the magnetoresistive-MEMS hybrid magnetic sensor

Soft magnetic alloy	Coercivity	Relative permeability	Thickness
$Co_{93}Zr_3Nb_4$[31]	0.75 Oe	853	350–400 nm
$(Co_{70}Fe_{30})_{80}B_{20}$[50]	4.7 Oe	203	680 nm
$Ni_{70}Fe_{30}$[25]	1.6 Oe	1700	1.2 μm
$Ni_{77}Fe_{14}Cu_5Mo_4$ (this work)	0.01 Oe	3246	400 nm

sensors. As can be seen from Table II, the MFC developed in this work exhibits a lower coercivity and a higher relative permeability, which endows the MTJ-MEMS hybrid magnetic sensor with significant advantages in sensitivity enhancement. In future research, process optimization strategies such as annealing treatment can be employed to relieve residual stresses within the Ta/$Ni_{77}Fe_{14}Cu_5Mo_4$ laminated structure. This stress relaxation not only improves the structural stability of the MFC but also provides the feasibility to further increase its thickness, which is expected to achieve a more pronounced magnetic flux focusing effect and thereby promote the overall performance of the sensor system.

After the optimization of the soft magnetic film structure and the identification of the best deposition conditions, a 400-nm-thick flux concentrator was deposited with AZ5214 photoresist as a mask. The AZ5214 photoresist offers better film release performance compared to conventional positive photoresists, facilitating the lift-off operation; meanwhile, the film deposition stages are conducted at room temperature. The sputtering power was set to 100 W, and the sputtering pressure was kept at 0.73 Pa. As shown in Fig. 10, a multi-step lift-off process was used to make MFCs. At first, MFCs with a thickness of 200 nm were deposited. After a successful lift-off, an additional 200 nm thick MFCs were deposited, which led to the final MFCs with a thickness of 400 nm. Through systematic experimental verification, we observed that when the thickness of the Ta (5 nm)/$Ni_{77}Fe_{14}Cu_5Mo_4$ (50 nm) stack exceeds 200 nm in a single lift-off process, the film is prone to tearing due to stress accumulation and poor adhesion compatibility. Thus, 200 nm was determined as the optimal single-stack deposition thickness. Additionally, further process exploration revealed that MFCs tend to peel off from the substrate when the total thickness exceeds 400 nm, which would compromise the structural stability and magnetic performance of the device. Based on these critical process constraints and performance validation, the final thickness of MFCs was set to 400 nm, achieved through two sequential 200 nm depositions. The contour of MFCs can be clearly seen in Fig. 11a. Both MFCs and MTJ had their processes optimized first, and then MFCs were combined with the MTJ, with a 12 μm space between the tip of MFCs and the MTJ.

The transfer curves of a single MTJ were measured before and after the deposition of MFCs. Figure 11b shows the device image with 200 nm thick integrated MFCs, along with the corresponding transfer curve. The sensitivity of the transfer curve at zero field (H = 0) increased from 6.1%/Oe to 9.4%/Oe, achieving a 1.5-fold gain. When the thickness of MFCs was increased to 400 nm (as shown in Fig. 11c), the sensitivity of the MTJ (H = 0) was further enhanced, reaching 13.5%/Oe, resulting in a 2.2-fold gain. The magnetic field gain of finite element simulation is 3.9, which is close to the measured value. Therefore, the prototype of this integrated device suggests that the TDSMM scheme is likely to be successfully validated.

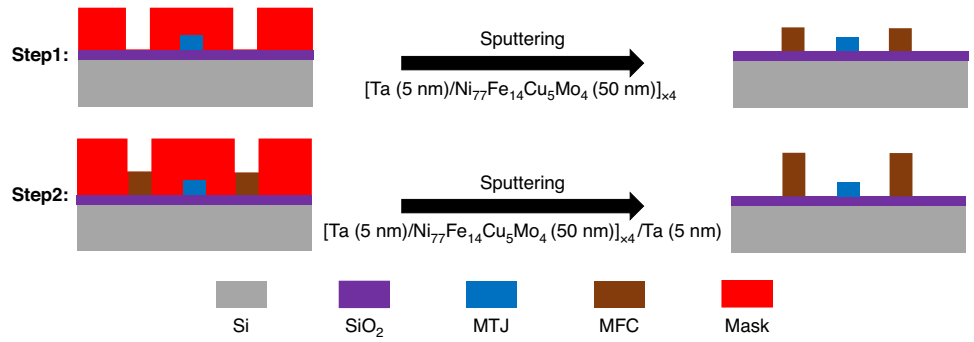

Fig. 10 Schematic diagram of the preparation of MFCs. The process flow diagram for integrating 400 nm thick MFCs on both sides of the MTJ

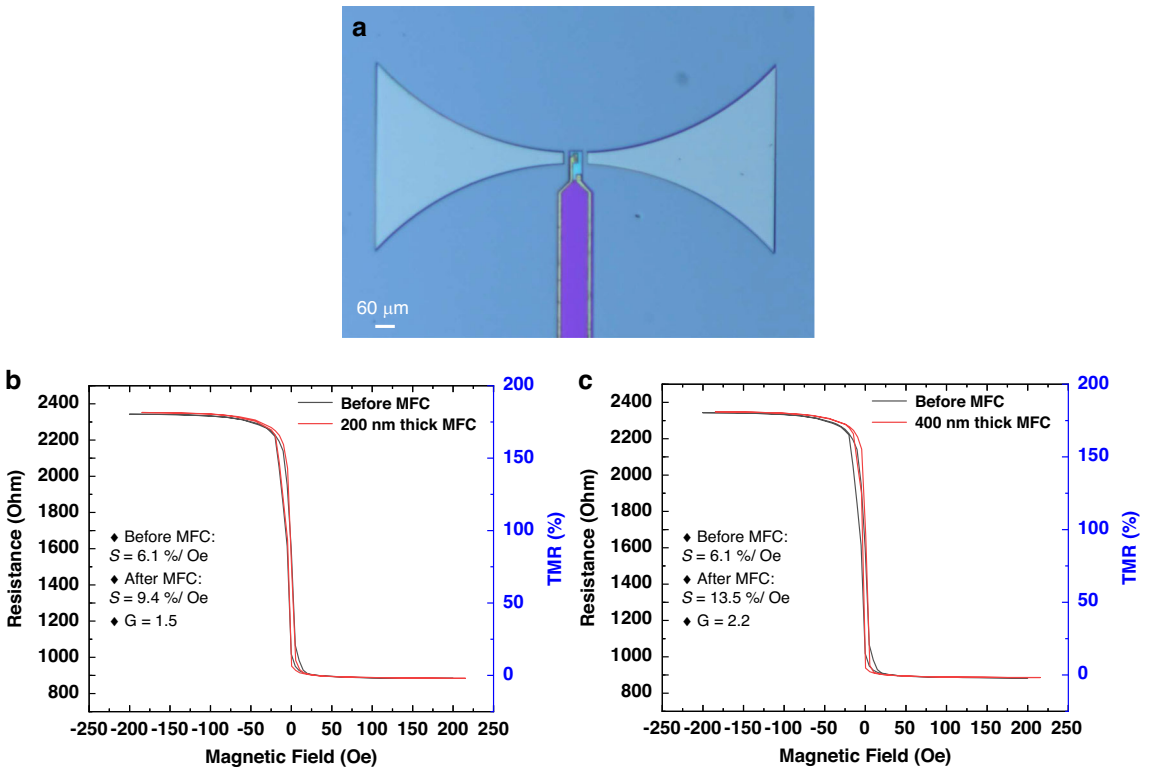

Fig. 11 The transfer curve of the MTJ sensor. a Microscopic image of 400 nm thick MFCs; **b** The transfer curve of MTJ integrated with 200 nm thick MFCs; **c** The transfer curve of MTJ integrated with 400 nm thick MFCs

The MTJ's noise was measured within a magnetic shielding box made up of six layers of permalloy alloy, which was able to effectively block external magnetic field interference. An SR560 low-noise preamplifier was utilized to amplify the MTJ output signal, and the noise of MTJ was measured by an SR785 spectrum analyzer. As shown in Fig. 12, when there is a 0.2 mA bias, the MTJ combined with MFCs exhibits a low-frequency noise of 2.4 μV/√Hz (at 1 Hz), which is equivalent to a detectivity of 10 nT/√Hz. The noise power spectral density is 3.5 nV/√Hz at 11,570 Hz, which is 686 times lower than that in the low - frequency range. As stated in ref.[36], the hybrid sensor's limit of detection (LOD) can be computed by means of the following formula:

$$LOD = \frac{S_v}{I_{bias} S_0 G E} \tag{3}$$

In formula (3), S_v represents the power spectral density in V/√Hz. I_{bias} represents the bias current of the MTJ element, and S_0 represents the sensitivity. Let G and

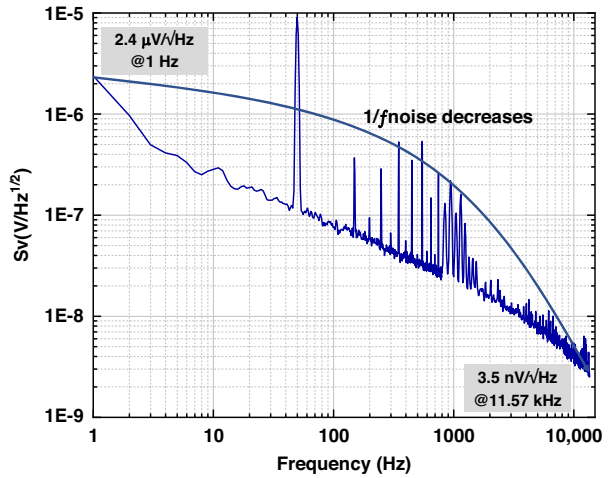

Fig. 12 The power spectral density of the MTJ sensor. Power spectral density of junction noise in the 400 nm MFC-coupled MTJ configuration with $I_{bias} = 0.2$ mA and $B_{ext} = 0$ mT

E respectively stand for the magnetic field gain of MFCs and the modulation efficiency of TDSMM. According to formula (3), it can be calculated that the future integration of MFCs with MTJs and TDSMM structures may potentially reduce the noise level of the MTJ element to the order of tens of pT, thereby significantly improving the magnetic field detectivity.

Conclusion

In this research, the development approach of the MTJ-MEMS magnetic sensor based on TDSMM was explored. The finite-element simulations showed that when the relative permeability of the magnetic film is over 600, the magnetic field in the gap of MFCs can be amplified effectively, which guarantees a high modulation efficiency for TDSMM. In addition, the modulation efficiency of TDSMM with MFCs which are 400 nm in thickness was simulated. The simulation result shows that its modulation efficiency is 65.4%, demonstrating a significant competitive advantage compared to other composite magnetoresistive sensors of similar type. A $Ni_{77}Fe_{14}Cu_5Mo_4$ laminated structure was adopted to successfully fabricate the magnetic film suitable for MFCs. Compared to a single-layer $Ni_{77}Fe_{14}Cu_5Mo_4$, the Ta (5 nm)/$Ni_{77}Fe_{14}Cu_5Mo_4$ (50 nm) laminated structure exhibited superior hysteresis loops, with a 10-fold reduction in coercivity. The effect of sputtering power on the hysteresis behavior of the magnetic film was studied, leading to the identification of the optimal deposition conditions for MFCs. At a sputtering power of 100 W, the magnetic film exhibited a relative permeability of 3246 along the easy axis, enabling MFCs to effectively amplify the magnetic field in the gap. By optimizing the fabrication process, 400 nm thick MFCs were successfully prepared and integrated with the MTJ, resulting in a sensor prototype with a gain of 2.2. The noise measurement of the MTJ integrated with MFCs revealed that the sensor's detectivity at 1 Hz was 10 nT/√Hz. Furthermore, at higher frequencies, the noise level of the sensor decreased by a factor of 686, indicating that the future integration of MEMS modulation structures has the potential to reduce the noise of MTJ elements to the order of tens of pT.

Acknowledgements

This work was supported in part by the National Key Research and Development Program of China (2023YFB2407800), the National Natural Science Foundation of China (Grant No. 62271469), Beijing Municipal Natural Science Foundation (Grant Number. L255006), the Lingang Laboratory (Grant No. LGL-5923-11), the Science and Disruptive Technology Program, the AIRCAS (2025-AIRCAS-SDTP-02), Young Elite Scientists Sponsorship Program by CAST (No. YESS20210341), the One Hundred Person Project of the Chinese Academy of Sciences, and the Xiaomi Young Talents Program.

Author details

[1]State Key Laboratory of Transducer Technology, Aerospace Information Research Institute, Chinese Academy of Sciences, Beijing 100190, China. [2]School of Electronic, Electrical and Communication Engineering, University of Chinese Academy of Sciences, Beijing 100049, China. [3]College of Materials Sciences and Opto-Electronic Technology, University of Chinese Academy of Sciences, Beijing 100049, China

Competing interests

The authors declare no competing interests.

Received: 6 August 2025 Revised: 5 December 2025 Accepted: 5 January 2026
Published online: 10 March 2026

References

1. Liu, Y. et al. Geomagnetism Aided Inertial Navigation System. *The 2008 2nd International Symposium on Systems and Control in Aerospace and Astronautics (ISSCAA)*, Shenzhen, China, https://doi.org/10.1109/ISSCAA.2008.4776291 (2008).
2. Poliakov, S. V., Reznikov, B. I., Shchennikov, A. V., Kopytenko, E. A. & Samsonov, B. V. The range of induction-coil magnetic field sensors for geophysical explorations. *Seismic Instrum.* **53**, 1–18 (2017).
3. Giebeler, C. et al. Robust GMR sensors for angle detection and rotation speed sensing. *Sens. Actuators A Phys.* **91**, 16–20 (2001).
4. Hiari, O. et al. Towards Single-Chip Diversity TMR for Automotive Applications. *The 2012 IEEE International Conference on Electro/Information Technology, Indianapolis*, USA, https://doi.org/10.1109/EIT.2012.6220736 (2012).
5. Cheung, S. Y. et al. Traffic measurement and vehicle classification with single magnetic sensor. *Transport. Res. Rec. J. Transport. Res. Board* **1917**, 173–181 (2005).
6. Martins, V. C. et al. Challenges and trends in the development of a magnetoresistive biochip portable platform. *J. Magn. Magn. Mater.* **322**, 1655–1663 (2010).
7. Pannetier-Lecoeur, M. et al. Magnetocardiography with sensors based on giant magnetoresistance. *Appl. Phys. Lett.* **98**, https://doi.org/10.1063/1.3575591 (2011).
8. Mujika, M. et al. Magnetoresistive immunosensor for the detection of Escherichia coli O157:H7 including a microfluidic network. *Biosens. Bioelectron.* **24**, 1253–1258 (2009).
9. Ger, T.-R., Huang, H.-T., Huang, C.-Y. & Lai, M.-F. Single cell detection using 3D magnetic rolled-up structures. *Lab a Chip* **13**, 4225 (2013).
10. Zhang, Y., Yan, Z., Zhu, J., Li, S. & Mi, C. A review of foreign object detection (FOD) for inductive power transfer systems. *eTransportation* **1**, 100002 (2019).

11. Oelsner, G., Schultze, V., Ijsselsteijn, R. & Stolz, R. Performance analysis of an optically pumped magnetometer in Earth's magnetic field. *EPJ Quantum Technol.* **6**, 6 (2019).
12. Mahdi, A. E., Panina, L. & Mapps, D. Some new horizons in magnetic sensing: high-Tc SQUIDs, GMR and GMI materials. *Sens. Actuators A Phys.* **105**, 271–285 (2003).
13. Shen, X., Teng, Y. & Hu, X. Design of a low-cost small-size fluxgate sensor. *Sensors* **21**, 6598 (2021).
14. Seo, M.-J. & Yoo, J.-C. Omnidirectional fingertip pressure sensor using Hall effect. *Sensors* **21**, 7072 (2021).
15. Wang, Z. et al. Highly sensitive flexible magnetic sensor based on anisotropic magnetoresistance effect. *Adv. Mater.* **28**, 9370–9377 (2016).
16. Amaral, J. et al. Measuring brain activity with magnetoresistive sensors integrated in micromachined probe needles. *Appl. Phys. A* **111**, 407–412 (2013).
17. Jin, Z., Wang, Y., Fujiwara, K., Oogane, M. & Ando, Y. Detection of small magnetic fields using serial magnetic tunnel junctions with various geometrical characteristics. *Sensors* **20**, 5704 (2020).
18. Jander, A., Nordman, C. A., Pohm, A. V. & Anderson, J. M. Chopping techniques for low-frequency nanotesla spin-dependent tunneling field sensors. *J. Appl. Phys.* **93**, 8382–8384 (2003).
19. Luong, V.-S. et al. Reduction of low-frequency noise in tunneling-magnetoresistance sensors with a modulated magnetic shielding. *IEEE Trans. Magn.* **50**, 1–4 (2014).
20. Luong, V. S., Jeng, J.-T., Lu, C.-C. & Hsu, H.-Y. Low-noise tunneling-magnetoresistance vector magnetometers with flux chopping technique. *Measurement* **109**, 297–303 (2017).
21. Shirotori, S., Kikitsu, A., Higashi, Y., Kurosaki, Y. & Iwasaki, H. Symmetric response magnetoresistance sensor with low 1/f noise by using an antiphase AC modulation bridge. *IEEE Trans. Magn.* **57**, 1–5 (2021).
22. Kikitsu, A. et al. Magnetic field microscope using high-sensitivity giant magneto-resistance sensor with AC field modulation. *Japanese J. Appl. Phys.* **62**, https://doi.org/10.35848/1347-4065/ac9145 (2022).
23. Pannetier, M., Fermon, C., Le Goff, G., Simola, J. & Kerr, E. Femtotesla magnetic field measurement with magnetoresistive sensors. *Science* **304**, 1648–1650 (2004).
24. Sun, K. et al. A superconductor/TMR composite magnetic sensor for pico-Tesla magnetic field detection. *AIP Adv.* **12**, https://doi.org/10.1063/5.0096826 (2022).
25. Hu, J. et al. Double-gap magnetic flux concentrator design for high-sensitivity magnetic tunnel junction sensors. *Sensors* **19**, 4475 (2019).
26. Feng, Y., Chen, J.-Y., Wu, K. & Wang, J.-P. Design and fabrication of integrated magnetic field sensing system with enhanced sensitivity. *J. Magn. Magn. Mater.* **511**, 166728 (2020).
27. Edelstein, A. S. & Fischer, G. A. Minimizing 1/f noise in magnetic sensors using a microelectromechanical system flux concentrator. *J. Appl. Phys.* **91**, 7795–7797 (2002).
28. Edelstein, A. S. et al. Progress toward a thousandfold reduction in 1/f noise in magnetic sensors using an ac microelectromechanical system flux concentrator (invited). *J. Appl. Phys.* **99**, https://doi.org/10.1063/1.2170067 (2006).
29. Ozbay, A. et al. Magnetic-field dependence of the noise in a magnetoresistive sensor having MEMS flux concentrators. *IEEE Trans. Magn.* **42**, 3306–3308 (2006).
30. Trindade, I. G. et al. High sensitivity spin valve sensors with AF coupled flux guides. *IEEE Trans. Magn.* **44**, 2472–2474 (2008).
31. Guedes, A., Almeida, J. M., Cardoso, S., Ferreira, R. & Freitas, P. P. Improving magnetic field detection limits of spin valve sensors using magnetic flux guide concentrators. *IEEE Trans. Magn.* **43**, 2376–2378 (2007).
32. Hu, J., Pan, M., Tian, W., Chen, D. & Luo, F. Integrating magnetoresistive sensors with microelectromechanical systems for noise reduction. *Appl. Phys. Lett.* **101**, https://doi.org/10.1063/1.4769903 (2012).
33. Hu, J. et al. Magnetoresistance based resonance monitoring with pulse-excited planar coils. *Appl. Phys. Lett.* **102**, https://doi.org/10.1063/1.4802756 (2013).
34. Guedes, A. et al. Hybrid magnetoresistive/microelectromechanical devices for static field modulation and sensor 1/f noise cancellation. *J. Appl. Phys.* **103**, https://doi.org/10.1063/1.2837661 (2008).
35. Guedes, A. et al. Towards picoTesla Magnetic Field Detection Using a GMR-MEMS Hybrid Device. *IEEE Trans. Magn.* **48**, 4115–4118 (2012).
36. Lyu, H. et al. A high-resolution MEMS magnetoresistive sensor utilizing magnetic tunnel junction motion modulation driven by the piezoelectric resonator. *Appl. Phys. Lett.* **121**, https://doi.org/10.1063/5.0109527 (2022).
37. Manyosa, X. et al. MEMS miniaturized low-noise magnetic field sensor for the observation of sub-millihertz magnetic fluctuations in space exploration. *Measurement* **230**, 114489 (2024).
38. Jiao, Q., Luo, J., Jin, Z., Zou, X. & Chen, J. Two-dimensional synchronous motion modulation MEMS structure for suppressing 1/f noise in magnetoresistive sensors. *AIP Adv.* **13**, https://doi.org/10.1063/5.0166463 (2023).
39. Guedes, A. et al. Hybrid magnetic tunnel junction-MEMS high frequency field modulator for 1/f noise suppression. *IEEE Trans. Magn.* **44**, 2554–2557 (2008).
40. Jiao, Q., Jin, Z., Zhang, C. & Chen, J. Various noise reduction techniques of magnetoresistive sensors and their applications: a review. *Measurement* **242**, 116143 (2025).
41. Ferreira, R., Paz, E., Freitas, P. P., Wang, J. & Xue, S. Large area and low aspect ratio linear magnetic tunnel junctions with a soft-pinned sensing layer. *IEEE Trans. Magn.* **48**, 3719–3722 (2012).
42. Djayaprawira, D. D. et al. 230% room-temperature magnetoresistance in CoFeB/MgO/CoFeB magnetic tunnel junctions. *Appl. Phys. Lett.* **86**, https://doi.org/10.1063/1.1871344 (2005).
43. Lopez-Dominguez, V. et al. A simple vibrating sample magnetometer for macroscopic samples. *Rev. Sci. Instrum.* **89**, https://doi.org/10.1063/1.5017708 (2018).
44. Trindade, I. G. et al. Linear field amplification for magnetoresistive sensors. *J. Appl. Phys.* **103**, https://doi.org/10.1063/1.2936315 (2008).
45. McCord, J. & Westwood, J. Domain optimization of sputtered permalloy shields for recording heads. *IEEE Trans. Magn.* **37**, 1755–1757 (2001).
46. Hubert, A. & Schäfer, R. Magnetic domains: the analysis of magnetic microstructures. (Springer Berlin Heidelberg, 2008).
47. Parkin, S. S. P. Systematic variation of the strength and oscillation period of indirect magnetic exchange coupling through the 3d, 4d, and 5d transition metals. *Phys. Rev. Lett.* **67**, 3598–3601 (1991).
48. Jovičević Klug, M. et al. Antiparallel exchange biased multilayers for low magnetic noise magnetic field sensors. *Appl. Phys. Lett.* **114**, https://doi.org/10.1063/1.5092942 (2019).
49. Guedes, A. et al. Hybrid GMR sensor detecting 950 pT/sqrt(Hz) at 1 Hz and room temperature. *Sensors* **18**, 790 (2018).
50. Leitao, D. C., Gameiro, L., Silva, A. V., Cardoso, S. & Freitas, P. P. Field detection in spin valve sensors using CoFeB/Ru synthetic-antiferromagnetic multilayers as magnetic flux concentrators. *IEEE Trans. Magn.* **48**, 3847–3850 (2012).